

KMT-2019-BLG-0797: binary-lensing event occurring on a binary stellar system

Cheongho Han¹, Chung-Uk Lee², Yoon-Hyun Ryu², Doeon Kim¹

(Leading authors),

Michael D. Albrow³, Sun-Ju Chung^{2,4}, Andrew Gould^{5,6}, Kyu-Ha Hwang², Youn Kil Jung², Hyoun-Woo Kim², In-Gu Shin², Yossi Shvartzvald⁷, Jennifer C. Yee⁸, Weicheng Zang⁹, Sang-Mok Cha^{2,10}, Dong-Jin Kim², Seung-Lee Kim^{2,4}, Dong-Joo Lee², Yongseok Lee^{2,10}, Byeong-Gon Park^{2,4}, and Richard W. Pogge⁶

(The KMTNet Collaboration),

¹ Department of Physics, Chungbuk National University, Cheongju 28644, Republic of Korea
e-mail: cheongho@astroph.chungbuk.ac.kr

² Korea Astronomy and Space Science Institute, Daejeon 34055, Republic of Korea

³ University of Canterbury, Department of Physics and Astronomy, Private Bag 4800, Christchurch 8020, New Zealand

⁴ Korea University of Science and Technology, 217 Gajeong-ro, Yuseong-gu, Daejeon, 34113, Republic of Korea

⁵ Max Planck Institute for Astronomy, Königstuhl 17, D-69117 Heidelberg, Germany

⁶ Department of Astronomy, The Ohio State University, 140 W. 18th Ave., Columbus, OH 43210, USA

⁷ Department of Particle Physics and Astrophysics, Weizmann Institute of Science, Rehovot 76100, Israel

⁸ Center for Astrophysics | Harvard & Smithsonian 60 Garden St., Cambridge, MA 02138, USA

⁹ Department of Astronomy, Tsinghua University, Beijing 100084, China

¹⁰ School of Space Research, Kyung Hee University, Yongin, Gyeonggi 17104, Republic of Korea

Received ; accepted

ABSTRACT

Aims. We analyze the microlensing event KMT-2019-BLG-0797. The light curve of the event exhibits two anomalous features from a single-lens single-source model, and we aim to reveal the nature of the anomaly.

Methods. It is found that a model with two lenses plus a single source (2L1S model) can explain one feature of the anomaly, but the other feature cannot be explained. We test various models and find that both anomalous features can be explained by introducing an extra source to a 2L1S model (2L2S model), making the event the third confirmed case of a 2L2S event, following on MOA-2010-BLG-117 and OGLE-2016-BLG-1003. It is estimated that the extra source comprises $\sim 4\%$ of the I -band flux from the primary source.

Results. Interpreting the event is subject to a close-wide degeneracy. According to the close solution, the lens is a binary consisting of two brown dwarfs with masses $(M_1, M_2) \sim (0.034, 0.021) M_\odot$, and it is located at a distance of $D_L \sim 8.2$ kpc. According to the wide solution, on the other hand, the lens is composed of an object at the star/brown-dwarf boundary and an M dwarf with masses $(M_1, M_2) \sim (0.06, 0.33) M_\odot$ located at $D_L \sim 7.7$ kpc. The source is composed of a late-G-dwarf/early-K-dwarf primary and an early-to-mid M-dwarf companion.

Key words. gravitational microlensing

1. Introduction

Microlensing light curves can exhibit deviations from the smooth and symmetric form of a single-lens single-source (1L1S) event. The most common causes for these anomalies are the binary nature of the lens, 2L1S event (Mao & Paczyński 1991), and the source, 1L2S event (Griest & Hu 1992). Detections of such three-object (2L+1S or 1L+2S) events by the first-generation lensing experiments, e.g., MACHO LMC 1 (Dominik & Hirschfeld 1994) and OGLE 7 (Udalski et al. 1994) 2L1S events and MACHO LMC 96-2 (Becker et al. 1997) 1L2S event, prompted theoretical studies on the lensing behavior under these lens system configurations. This led to the establishment of observational strategies for efficient detections of microlensing anomalies, e.g., survey+follow-up mode observations for intensive coverage of short-lasting anomalies (Gould & Loeb 1992), and the development of methodologies for efficient analyses of

anomalous lensing events, e.g., ray-shooting method (Bond et al. 2002; Dong et al. 2009; Bennett et al. 2010) and contour integration algorithm (Gould & Gauchetel 1997; Bozza et al. 2018). Thanks to the accomplishments on both observational and theoretical sides, more than a hundred anomalous events are currently being detected each year, and they are promptly analyzed almost in real time with the progress of events (Ryu et al. 2010; Bozza et al. 2012).

With the great increase of the event detection rate together with the dense coverage of lensing light curves by high-cadence lensing surveys, OGLE-IV (Udalski et al. 2015), MOA (Bond et al. 2001), and KMTNet (Kim et al. 2016), one is occasionally confronted with events for which observed lensing light curves cannot be explained by interpretations with three objects. At the time of writing this article, there exist thirteen confirmed cases of events, for which at least four objects (lenses plus sources) are required to interpret observed light

Table 1. Microlensing events with more than four bodies

| Model | Event | Reference |
|-----------------------------|--------------------|--|
| 3L1S (planet in binary) | OGLE-2008-BLG-092 | Poleski et al. (2014) |
| | OGLE-2007-BLG-349 | Bennett et al. (2016) |
| | OGLE-2013-BLG-0341 | Gould et al. (2014) |
| | OGLE-2016-BLG-0613 | Han et al. (2017) |
| | OGLE-2018-BLG-1700 | Han et al. (2020b) |
| | OGLE-2019-BLG-0304 | Han et al. (2020g) |
| 3L1S (two-planet system) | OGLE-2006-BLG-109 | Gaudi et al. (2008); Bennett et al. (2010) |
| | OGLE-2012-BLG-0026 | Han et al. (2013) |
| | OGLE-2018-BLG-1011 | Han et al. (2019) |
| 1L3S | OGLE-2015-BLG-1459 | Hwang et al. (2018) |
| 2L2S | MOA-2010-BLG-117 | Bennett et al. (2018) |
| | OGLE-2016-BLG-1003 | Jung et al. (2017) |
| 3L2S | KMT-2019-BLG-1715 | Han et al. (2020e) |
| 3L1S or 2L2S | OGLE-2014-BLG-1722 | Suzuki et al. (2018) |
| | OGLE-2018-BLG-0532 | Ryu et al. (2020) |
| | KMT-2019-BLG-1953 | Han et al. (2020a) |

curves. These events are listed in Table 1. Nine of these are 3L1S events, in which the lensing system is composed of three lens masses and a single source star. Among them, the lenses of six events (OGLE-2008-BLG-092, OGLE-2007-BLG-349, OGLE-2013-BLG-0341, OGLE-2016-BLG-0613, OGLE-2018-BLG-1700, and OGLE-2019-BLG-0304) are planets in binaries, and the lenses of the other three events (OGLE-2006-BLG-109, OGLE-2012-BLG-0026, OGLE-2018-BLG-1011) are systems containing two planets. The lensing event OGLE-2015-BLG-1459 was identified as a 1L3S event, in which a single-lens mass was involved with three source stars. The events MOA-2010-BLG-117 and OGLE-2016-BLG-1003 were very rare cases, in which both the lens and source are binaries. Interpretation of the event KMT-2019-BLG-1715 is even more complex and requires five objects, in which the lens is composed of three masses (a planet plus two stars) and the source consists of two stars, that is, 3L2S event. Besides these events, there exist three additional events (OGLE-2014-BLG-1722, OGLE-2018-BLG-0532, and KMT-2019-BLG-1953), in which four-object modeling is required to explain the observed light curves, but unique solutions cannot be firmly specified due to either degeneracies among different interpretations or not enough coverage of signals. Accumulation of knowledge from modeling these multi-body events is important for future interpretations of lensing light curves with complex anomalous features.

In this paper, we present the analysis of the lensing event KMT-2019-BLG-0797. The light curve of the event exhibits two anomalous features, which cannot be explained by a usual 2L1S or 1L2S model. We test various four-object models, in which an extra lens or source are considered in the interpretation of the event.

The anomalous nature of KMT-2019-BLG-0797 was found from a project conducted to reanalyze previous KMTNet events detected in and before the 2019 season. In the first part of this project, Han et al. (2020d) investigated events involved with faint source stars and found four planetary events (KMT-2016-BLG-2364, KMT-2016-BLG-2397, OGLE-2017-BLG-0604, and OGLE-2017-BLG-1375), for which no detailed investigation had been conducted. The second part of the project was focused on high-magnification events, aiming to find subtle planetary signals, and this led to the discoveries of two planetary systems KMT-2018-BLG-0748L (Han et al. 2020c) and KMT-2018-BLG-1025L (Han et al. 2020h). The event KMT-2019-BLG-0797 was closely examined as a part of the project in-

vestigating high-magnification events involved with faint source stars.

For the presentation of the work, we organize the paper as follows. In Sect. 2, we mention the data of the lensing event analyzed in this work and describe observations conducted to acquire the data. In Sect. 3, we depict the anomaly that appeared on the light curve and describe various tests conducted to interpret the anomaly. We estimate the angular Einstein radius of the lensing event in Sect. 4, and estimate the physical parameters of the lens and source in Sect. 5. We summarize the results and conclude in Sect. 6.

2. Observation and data

The lensing event KMT-2019-BLG-0797 occurred on a source lying toward the Galactic bulge. The equatorial and galactic coordinates of the source are $(RA, DEC)_{J2000} = (17 : 53 : 48.09, -31 : 58 : 36.70)$ and $(l, b) = (-1^\circ.706, -3^\circ.073)$, respectively. The brightness of the source had remained constant with an apparent baseline brightness of $I_{\text{base}} \sim 20.1$, as measured on the KMTNet scale, before the lensing magnification. The lensing-induced magnification of the source flux lasted about 10 days as measured by the duration beyond the photometric scatter.

The event was detected on 2019 May 13 ($HJD' \equiv HJD - 2450000 \sim 8616.6$) by the Alert Finder System (Kim et al. 2018) of the KMTNet survey. The survey uses three identical wide-field telescopes that are globally located in three continents. The locations of the individual telescopes are the Siding Spring Observatory (KMTA) in Australia, the Cerro Tololo Inter-American Observatory (KMTC) in South America, and the South African Astronomical Observatory (KMST) in Africa. Each KMTNet telescope has a 1.6m aperture and is equipped with a camera yielding $2^\circ \times 2^\circ$ field of view. Images of the source were mainly acquired in the I band, and about one tenth of images were obtained in the V band for the source color measurement. We will describe the detailed procedure of determining the source color in Sect. 4.

Figure 1 shows the lensing light curve of KMT-2019-BLG-0797. The curve plotted over the data points is a 1L1S model with $(t_0, u_0, t_E) \sim (8617.06, 0.20, 4.6 \text{ days})$, where the individual lensing parameters indicate the peak time, impact parameter of the lens-source approach (normalized to the angular Einstein radius θ_E), and event timescale, respectively. The inset shows the zoomed-in view of the peak region, around which the data ex-

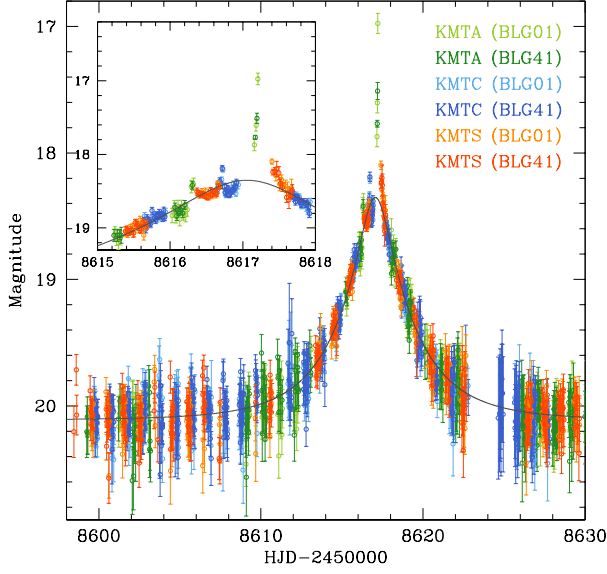


Fig. 1. Light curve of KMT-2019-BLG-0797. The curve drawn over the data points is a 1L1S model. The inset shows the region around the peak. The colors of the data points match those of the telescopes, marked in the legend, used to acquire the data.

hibit an anomaly relative to the 1L1S model. The date of the event alert approximately corresponds to the peak of the lensing magnification. The anomaly was already in progress at the time of the event alert, but it was not noticed due to the subtlety of the anomaly together with the considerable photometric uncertainties of data caused by the faintness of the source. As a result, little attention was paid to the event when the event was found, and thus no alert for follow-up observations was issued. Nevertheless, the peak region of the light curve was densely and continuously covered, because the source was located in the two overlapping KMTNet fields of BLG01 and BLG41, toward which observations were conducted most frequently. The observational cadence for each field was 30 min, and thus the event was covered with a combined cadence of 15 min.

Photometry of the event was conducted utilizing the KMT-Net pipeline (Albrow et al. 2009), which is a customized version of pySIS code developed on the basis of the difference imaging method (Tomaney & Crofts 1996; Alard & Lupton 1998). Additional photometry is conducted for a subset of KMTNet *I*- and *V*-band data using the pyDIA software (Albrow 2017) to measure the color of the source and to construct a color-magnitude diagram (CMD) of ambient stars around the source. We readjust error bars of data estimated from the pipeline following the standard routine described in Yee et al. (2012).

3. Anomaly

Figure 2 shows the detailed pattern of the anomaly in the peak region. It shows that the anomaly consists of two distinctive features. The first is the caustic-crossing feature, which is composed of two spikes at $\text{HJD}' \sim 8616.3$ and 8616.7 and the U-shape trough between the spikes. The other feature is the strong positive deviation from the 1L1S model centered at $\text{HJD}' \sim 8617.2$. The KMTA data partially cover the rising side of the second fea-

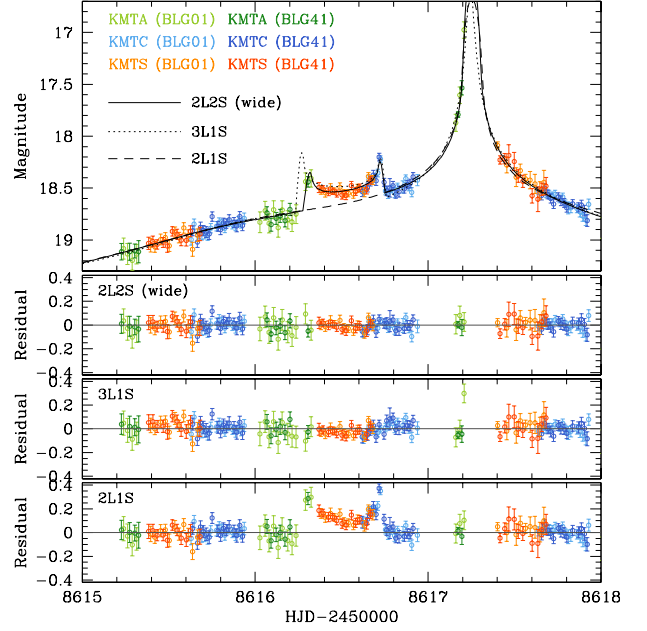


Fig. 2. Zoomed-in view around the peak of the light curve. Drawn over the data points are the 2L2S (wide), 3L1S, and 2L1S models. The lower three panels show the residuals from the individual models.

ture, but the falling side was not covered until almost the end of the anomaly.

3.1. 2L1S model

Considering that both anomalous features are likely to be involved with source star's crossing over or approaching a caustic, we first model the observed light curve under the assumption that the lens is a binary. In addition to the 1L1S lensing parameters, a 2L1S modeling requires one to include the three additional parameters (s, q, α), which represent the projected separation (normalized to θ_E), mass ratio between the binary lens components, M_1 and M_2 , and the angle between the source trajectory and the M_1 - M_2 axis (source trajectory angle), respectively. In the 2L1S modeling, we conduct thorough grid searches for the binary parameters (s, q) with multiple starting points of α evenly distributed in the range of $0 \leq \alpha \leq 2\pi$. For the computations of finite-source magnifications, we use the ray-shooting method described in Dong et al. (2009). From this investigation, we find that the 2L1S modeling does not yield a plausible model explaining the observed anomalous features.

We then conduct another 2L1S modeling, this time, by excluding the data around one of the two anomaly features. The modeling conducted by removing the data around the second anomalous feature does not yield a reasonable solution either.¹ However, the modeling with the exclusion of the first anomalous feature yields a solution that well describes the second anomalous feature.

¹ As we will show in the following subsection, the first anomalous feature is produced by an extra source. This source comprises a very minor fraction of the primary source, and the most flux comes from the primary source. As a result, the contribution of the second source to the lensing light curve is confined only to the time of the first anomaly, and thus the 2L1S modeling conducted excluding the second anomalous feature does not yield a model describing the overall light curve.

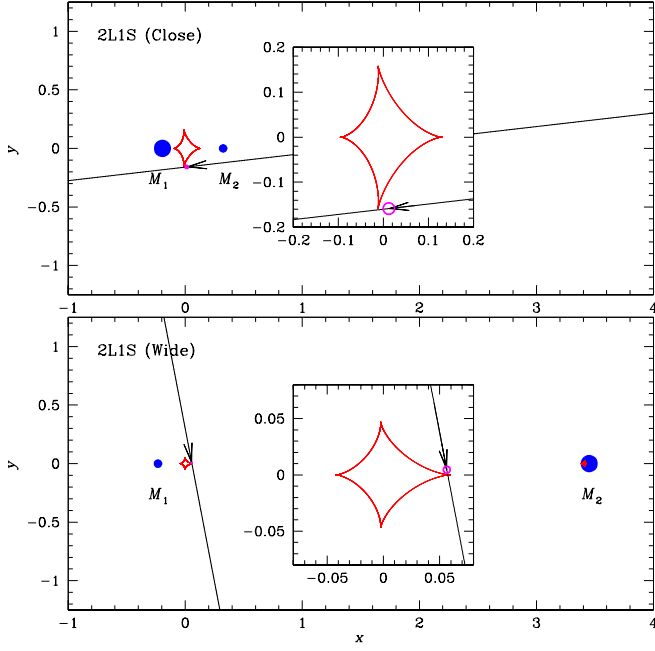


Fig. 3. Lens system configurations of the 2L1S solutions. The upper and lower panels are for the close and wide solutions, respectively. The inset in each panel shows the enlarged view around the caustic located close to the source trajectory (line with an arrow). The blue dots marked by M_1 and M_2 denote the positions of the binary lens components, and the bigger dot represents the heavier lens mass. Lengths are scaled to the Einstein radius. The small magenta circle on the source trajectory represents the source size scaled to the Einstein radius: $\rho = \theta_s / \theta_E$.

Table 2. Best-fit parameters of 2L1S solutions

| Parameter | Close | Wide |
|------------------------------|----------------------|-------------------------------------|
| t_0 (HJD') | 8617.114 ± 0.007 | 8617.103 ± 0.007 |
| u_0 / u'_0 | 0.159 ± 0.005 | $0.059 \pm 0.004 / 0.154 \pm 0.011$ |
| t_E / t'_E (days) | 4.64 ± 0.09 | $12.56 \pm 0.66 / 4.83 \pm 0.26$ |
| s | 0.519 ± 0.008 | 3.628 ± 0.051 |
| q | 0.599 ± 0.068 | 5.753 ± 0.705 |
| α (rad) | 6.168 ± 0.013 | 4.524 ± 0.010 |
| ρ / ρ' (10^{-3}) | 12.72 ± 1.73 | $3.00 \pm 0.69 / 7.81 \pm 1.82$ |

Notes. HJD' \equiv HJD – 2450000. The parameters (u'_0, t'_E, ρ') of the wide solution are the values scaled to the angular Einstein radius corresponding to M_1 , i.e., $\theta'_E = \theta_E / (1 + q)^{1/2}$.

The model curve of the 2L1S solution obtained by excluding the first anomalous feature is plotted over the data points in Figure 2, and the lensing parameters of the solution are listed in Table 2. We find two sets of solutions, in which one has a binary separation smaller than unity ($s < 1.0$) and the other solution has a separation greater than unity ($s > 1.0$). We refer to the two solutions as the “close” and “wide” solutions, respectively. The binary parameters of the close and wide solutions are $(s, q, \alpha)_{\text{close}} \sim (0.52, 0.60, -6.6^\circ)$ and $(s, q, \alpha)_{\text{wide}} \sim (3.62, 5.75, -100.8^\circ)$, respectively. We note that M_1 denotes the lens component located closer to the source trajectory, not the heavier mass component, and thus the mass ratio q of the wide solution is greater than unity. For the wide solution, we present additional parameters (u'_0, t'_E, ρ'), which represent the values scaled to the angular Einstein radius corresponding to M_1 , $\theta'_E = \theta_E / (1 + q)^{1/2}$, and thus $u'_0 = u_0(1 + q)^{1/2}$, $t'_E = t_E / (1 + q)^{1/2}$, and $\rho' = \rho(1 + q)^{1/2}$. It is found that the parameters (u'_0, t'_E, ρ') of

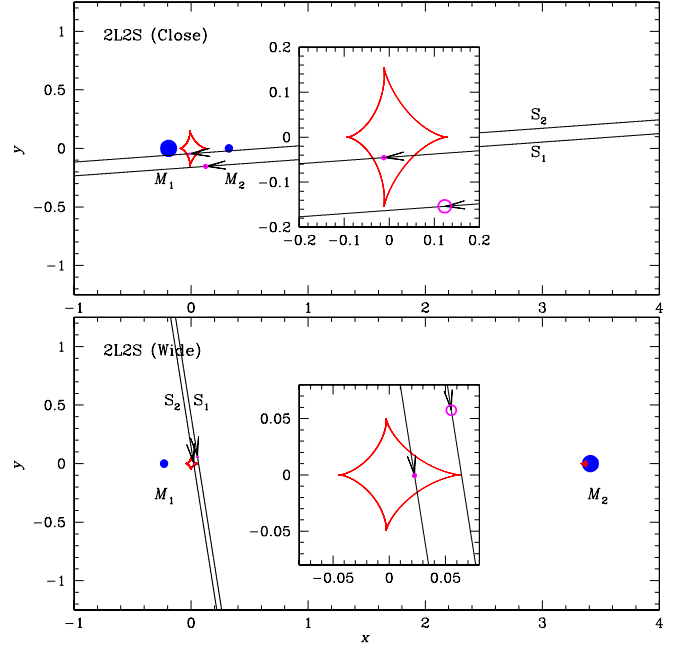


Fig. 4. Lens system configuration of the 2L2S model. Notations are same as those in Fig. 3 except that there is an additional source trajectory of the second source, S_2 .

Table 3. Best-fit parameters of 2L2S solutions

| Parameter | Close | Wide |
|----------------------------------|----------------------|-------------------------------------|
| χ^2 | 1907.2 | 1901.7 |
| $t_{0,1}$ (HJD') | 8617.145 ± 0.008 | 8617.132 ± 0.006 |
| $u_{0,1} / u'_{0,1}$ | 0.162 ± 0.006 | $0.063 \pm 0.003 / 0.158 \pm 0.005$ |
| $t_{0,2}$ (HJD') | 8616.549 ± 0.007 | 8616.500 ± 0.005 |
| $u_{0,2} / u'_{0,2}$ | 0.045 ± 0.002 | $0.022 \pm 0.001 / 0.055 \pm 0.003$ |
| t_E / t'_E (days) | 4.68 ± 0.08 | $12.08 \pm 0.35 / 4.82 \pm 0.14$ |
| s | 0.515 ± 0.008 | 3.641 ± 0.042 |
| q | 0.595 ± 0.052 | 5.259 ± 0.387 |
| α (rad) | 6.211 ± 0.011 | 4.556 ± 0.009 |
| ρ_1 / ρ'_1 (10^{-3}) | 14.24 ± 2.33 | $4.38 \pm 0.45 / 10.96 \pm 1.13$ |
| ρ_2 / ρ'_2 (10^{-3}) | 3.99 ± 0.50 | $1.45 \pm 0.19 / 3.63 \pm 0.48$ |
| q_{EJ} | 0.040 ± 0.003 | 0.043 ± 0.003 |

the wide solution are similar to the corresponding parameters of the close solution.

Figure 3 shows the configuration of the lens system corresponding to the 2L1S solutions. The upper and lower panels are the configurations of the close and wide solutions, respectively. According to these solutions, the second feature of the anomaly is produced by the source crossing over the tip of the four-cusp caustic induced by a binary. We note that the binary separation, $s \sim 0.52$ for the close solution and $s \sim 2.6$ for the wide solution, of the lens is neither much smaller nor much greater than unity, and thus the lens system is not in the regime of the Chang-Refsdal (C-R) lensing, which refers to the gravitational lensing of a point mass perturbed by a constant external shear (Chang & Refsdal 1979, 1984). As a result, the caustic slightly deviates from the symmetric astroid shape of the C-R lensing caustic. The source crosses the caustic tip located on the long side of the caustic

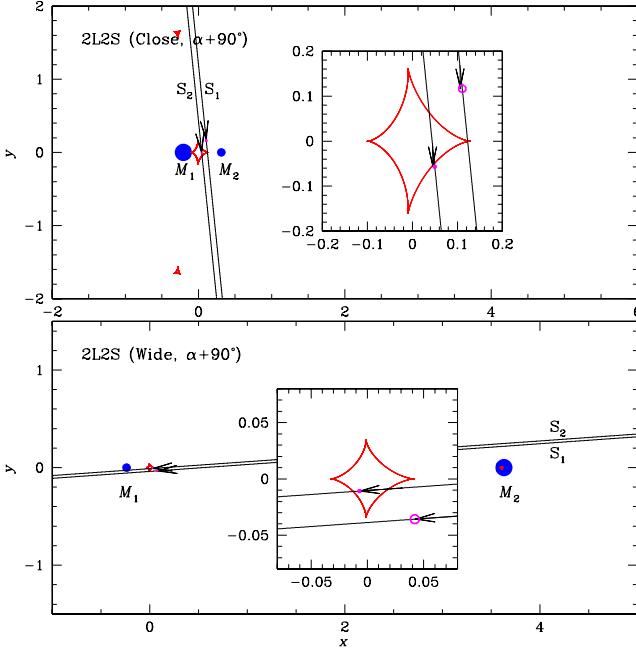


Fig. 5. Lens system configuration of the models obtained by confining the source trajectory angle around $\sim \alpha + 90^\circ$ from the best-fit solutions with α .

3.2. 2L2S model

We conduct another modeling under the interpretation that both the lens and source are binaries (2L2S model). The lensing magnification of a 2L2S event is the superposition of those involved with the individual source stars, S_1 and S_2 , that is,

$$A = \frac{A_1 F_{S_1} + A_2 F_{S_2}}{F_{S_1} + F_{S_2}} = \frac{A_1 + A_2 q_F}{1 + q_F}. \quad (1)$$

Here (F_{S_1}, F_{S_2}) and (A_1, A_2) denote the baseline flux values and the magnifications associated with the individual source stars, respectively, and $q_F = F_{S_2}/F_{S_1}$ represents the flux ratio between the source stars. The consideration of an extra source requires one to include additional parameters in modeling. These parameters are $(t_{0,2}, u_{0,2}, \rho_2, q_F)$, which represent the time of the closest approach of S_2 to the lens, and the lens-source separation at that time, the normalized radius of S_2 , and the flux ratio between S_1 and S_2 , respectively (Hwang et al. 2013). As initial values of the parameters related to the S_1 , $(t_{0,1}, u_{0,1}, t_E, s, q, \alpha, \rho_1)$, we use the values obtained from the 2L1S modeling. We set the initial values of $(t_{0,2}, u_{0,2}, \rho_2, q_F)$ considering the time and strength of the first anomaly feature.

It is found that the 2L2S modeling yields solutions that well describe the observed data including both anomalous features. We find two sets of solutions resulting from the close-wide degeneracy, and the best-fit lensing parameters of the individual solutions are listed in Table 3. It is found that the wide solution yields a slightly better fit to the data than the close solution, especially in the region around the second anomalous feature. However, the χ^2 difference between the two solutions is merely $\Delta\chi^2 = 5.5$, and thus we consider the close solution as a viable model. The model curves of the wide solution and the residual from the model are shown in Figure 2.

In Figure 4, we present the lens system configurations corresponding to the close (upper panel) and wide (lower panel) 2L2S solutions. From the comparison of the lensing parameters with

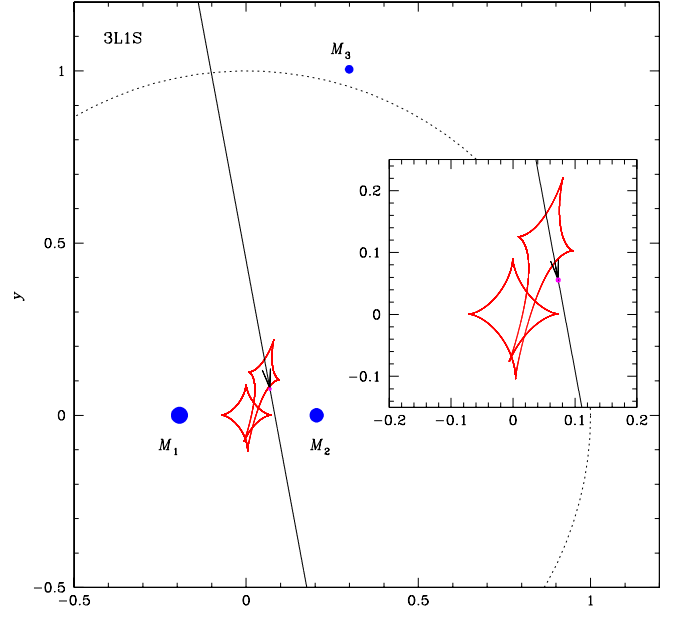


Fig. 6. Lens system configuration of the 3L1S model. We note that there are three lens components, marked by M_1 , M_2 , and M_3 . The dotted circle with a radius unity and centered at the M_1 – M_2 barycenter represents the Einstein ring.

Table 4. Best-fit parameters of 3L1S solution

| Parameter | Value |
|----------------------|----------------------|
| χ^2 | 2028.6 |
| t_0 (HJD') | 8617.159 ± 0.006 |
| u_0 | 0.082 ± 0.004 |
| t_E (days) | 6.03 ± 0.22 |
| s_2 | 0.398 ± 0.008 |
| q_2 | 0.947 ± 0.064 |
| α (rad) | 4.529 ± 0.011 |
| s_3 | 1.119 ± 0.006 |
| q_3 (10^{-3}) | 2.75 ± 0.28 |
| ψ (rad) | 1.115 ± 0.011 |
| ρ (10^{-3}) | 2.70 ± 0.37 |

those of the 2L1S solutions, presented in Table 2, it is found that the parameters related to S_1 ($t_{0,1}, u_{0,1}, t_E, s, q, \alpha$) for the 2L1S and 2L2S solutions are similar to each other. The main difference between the two solutions is the presence of an additional source S_2 that approaches M_1 closer than S_1 does. The second source passes over the caustic producing a caustic-crossing feature in the light curve, and this explains the first anomalous feature that could not be explained by the 2L1S model. According to the 2L2S solutions, the companion source comprises about 4% of the I -band flux from the primary source, that is, $q_{F,I} \sim 0.04$.

We note that the source trajectory of the event is well constrained despite the approximately symmetric shape of the caustic. For a binary lens in a C-R lensing regime, the induced caustic has a symmetric astroid shape with four cusps. In this case, the lensing light curves resulting from the source trajectory angles α and $\alpha \pm 90^\circ$ have a similar shape. See Figure 4 of Hwang et al. (2010) for the illustration of this degeneracy. We find that KMT-2019-BLG-0797 is not subject to this degeneracy because the source trajectory of the solution with $\alpha \pm 90^\circ$ is approximately aligned with the line connecting the central and peripheral caustics of the binary lens. To demonstrate this, in Figure 5, we plot

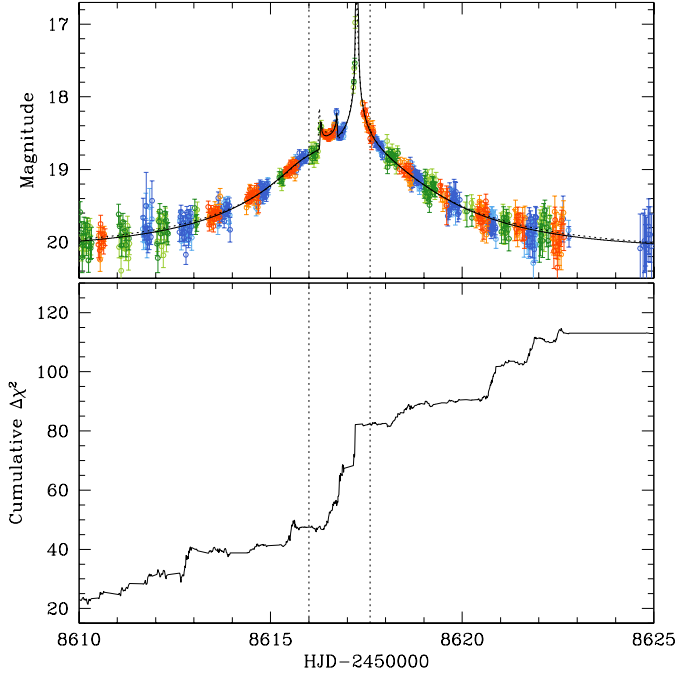


Fig. 7. Cumulative distribution of χ^2 difference between the 3L1S and 2L2S models, that is, $\Delta\chi^2 = \chi^2_{3L1S} - \chi^2_{2L2S}$. The two dotted vertical lines are drawn to indicate the region of the anomalies.

the lens system configurations of the solutions obtained by confining the source trajectory angle around $\sim \alpha \pm 90^\circ$ from the best-fit solution. It shows that these solutions result in source trajectories passing close to the peripheral caustic lying away from the central caustic. The source approach to the peripheral caustic results in an additional bump in the lensing light curve before the main peak. To avoid such a bump, the source trajectory angle of these solutions has less freedom in α , and this leads to a worse fit than the solutions presented in Table 3.

3.3. 3L1S model

We also test a model, in which the lens has three components (3L1S model). We test this model because the anomalous features appear around the peak of the light curve, and thus a third mass, if it exists, may induce an additional caustic and explain the first anomalous feature that is not explained by a 2L1S model, for example, OGLE-2016-BLG-0613 (Han et al. 2017), OGLE-2018-BLG-1700 (Han et al. 2020f), OGLE-2019-BLG-0304 (Han et al. 2020g). In the 3L1S modeling, we conduct a thorough grid search for the parameters describing the third lens mass, M_3 . These parameters include (s_3, q_3, ψ) , which denote the normalized M_1 – M_3 separation, mass ratio $q_3 = M_3/M_1$, and the position angle of M_3 as measured from the M_1 – M_2 axis and with a center at M_1 .

The 3L1S modeling also yields a solution that appears to depict both anomalous features. In Figure 2, we present the model curve and residual in the peak region of the light curve. The best-fit lensing parameters of the model are listed in Table 4, and the corresponding lens system configuration is shown in Figure 6. According to this solution, the first anomalous feature is produced by the crossing of the source over an additional caustic induced by a low-mass third lens component. The estimated mass ratio of the third mass to the primary is $q_3 = M_3/M_1 = (2.75 \pm 0.28) \times 10^{-3}$, indicating that M_3 is a planetary mass object.

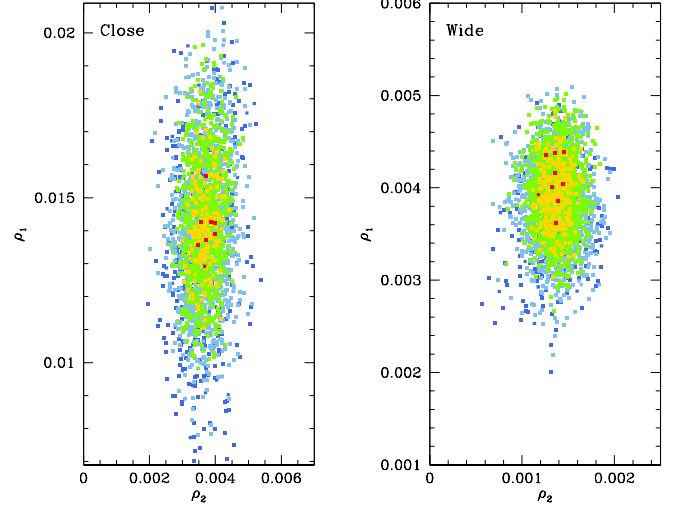


Fig. 8. Scatter plots in the MCMC chain on the ρ_1 – ρ_2 parameter plane for the close (left panel) and wide (right panel) solutions. The color coding is set to indicate points within 1σ (red), 2σ (yellow), 3σ (green), 4σ (cyan), and 5σ (blue).

The planet is located close to the Einstein ring corresponding to $M_1 + M_2$ with a position angle of $\psi \sim 64^\circ$. Due to the proximity of s_3 to unity, the planet induces a single large resonant caustic, and the source passes through the planet-induced caustic, producing the first anomalous feature, before it approaches the cusp of the binary-induced caustic, producing the second anomalous feature.

Although the 3L1S model seemingly describes the anomalous features, it is found that the model fit is substantially worse than the 2L2S model. The difference in the fits between the two models as measured by χ^2 difference is $\Delta\chi^2 = \chi^2_{3L1S} - \chi^2_{2L2S} = 126.9$, indicating that the 2L2S model is strongly preferred over the 3L1S model. To show the difference in the fits, we present the cumulative distribution of $\Delta\chi^2$ between the two models in Figure 7. The distribution shows that the 2L2S model provides a better fit than the 3L1S model not only in the region around the peak but also throughout the lightcurve during the lensing magnification.

4. Angular Einstein radius

In this section, we estimate the angular Einstein radius θ_E . In order to estimate θ_E , it is required to measure the normalized source radius, that is related to the angular Einstein radius by

$$\theta_E = \frac{\theta_*}{\rho}. \quad (2)$$

Here θ_* represents the angular source radius. We find that the normalized source radii of both S_1 and S_2 are constrained, although the uncertainties are considerable due to a partial coverage of the caustic crossings. This can be seen in Figure 8, in which we present scatter plots of the points in the MCMC chain on the ρ_1 – ρ_2 parameter plane for the close (left panel) and wide (right panel) solutions. We note that the uncertainty of ρ_1 is greater than the uncertainty of ρ_2 , because only the rising part of the second anomalous feature was covered by the data.

Another requirement for the θ_E measurement is estimating the angular source radius θ_* . We estimate θ_* from the color and brightness of the source. In order to estimate calibrated color

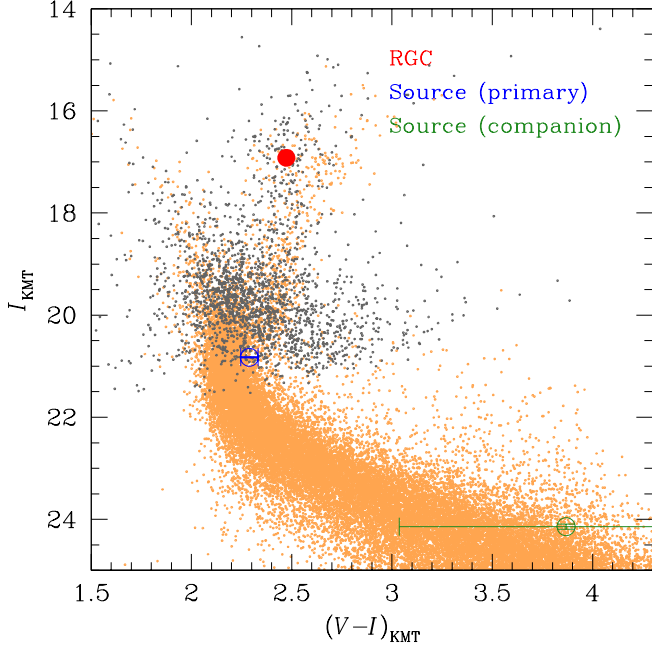


Fig. 9. Locations of the primary and companion source stars with respect to the centroid of the red giant clump (RGC) in the instrumental color-magnitude diagram (CMD, grey dots). The determinations of the source positions and the construction of the CMD are based on the pyDIA photometry of the KMTC data set. We also present the *Hubble Space Telescope* CMD (Holtzman et al. 1998, brown dots) to show the source locations on the main-sequence branch.

Table 5. Source color and magnitude

| Quantity | Value |
|------------------------|---------------------------------------|
| $(V-I)_{\text{RGC}}$ | (2.473, 16.918) |
| $(V-I)_{\text{RGC},0}$ | (1.060, 14.509) |
| primary (S_1) | |
| $(V-I, I)$ | $(2.289 \pm 0.043, 20.827 \pm 0.010)$ |
| $(V-I, I)_0$ | $(0.876 \pm 0.043, 18.418 \pm 0.010)$ |
| companion (S_2) | |
| $(V-I, I)$ | $(3.868 \pm 0.831, 24.143 \pm 0.053)$ |
| $(V-I, I)_0$ | $(2.455 \pm 0.831, 21.734 \pm 0.053)$ |

and brightness from the instrumental values, we use the method of Yoo et al. (2004). In this method, the centroid of red giant clump (RGC), with its known de-reddened color and magnitude, in the CMD serves as a reference for the color and magnitude calibration.

In the first step of the method, we estimate the combined (instrumental) flux from the source stars, $F_{S,p} = F_{S_1,p} + F_{S_2,p}$, and the companion/primary flux ratio, $q_{F,p}$, by fitting the KMTC photometry data set processed using the pyDIA code. Here the subscript “p” denotes the passband of observation. The measured values are $(F_{S,I}, F_{S,V}) = (0.07751 \pm 0.00060, 0.00909 \pm 0.00032)$ and $(q_{F,I}, q_{F,V}) = (0.0471 \pm 0.0023, 0.0110 \pm 0.0084)$. We note that the value of $q_{F,I}$, which is derived from the pyDIA reduction, is slightly different (less than 1σ) from the value presented in Table 3, which is derived from the pySIS reduction, because they come from different reductions of the data. Then, the flux values from S_1 and S_2 are estimated by

$$F_{S_1,p} = \left(\frac{1}{1 + q_{F,p}} \right) F_{S,p}; \quad F_{S_2,p} = \left(\frac{q_{F,p}}{1 + q_{F,p}} \right) F_{S,p}, \quad (3)$$

Table 6. Angular source radius, Einstein radius, and proper motion

| Quantity | Close | Wide |
|-------------------------------|-------------------|-------------------------------------|
| θ_* (μas) | 0.803 ± 0.066 | ← |
| θ_E / θ'_E (mas) | 0.056 ± 0.005 | $0.183 \pm 0.015 / 0.073 \pm 0.006$ |
| μ (mas yr $^{-1}$) | 4.40 ± 0.36 | 5.54 ± 0.46 |

Notes. The notation “←” in the wide solution column implies that the value is same as the one in the left column.

respectively. From the measured flux values in the I and V bands, it is estimated that the colors and magnitudes of S_1 and S_2 are $(V-I, I)_{S_1} = (2.289 \pm 0.043, 20.827 \pm 0.010)$ and $(V-I, I)_{S_2} = (3.868 \pm 0.831, 24.143 \pm 0.053)$, respectively. In Figure 9, we mark the locations of S_1 and S_2 with respect to the RGC centroid in the instrumental CMD constructed using the pyDIA photometry of the KMTC data (grey dots).

Although the V -band flux of S_2 has a relatively large *fractional* (i.e., magnitude) error, it is strongly constrained to be faint in an absolute sense. In particular, we find

$$q_{F,I} - q_{F,V} = 0.0381 \pm 0.0087, \quad (4)$$

i.e., a 4.4σ difference. This serves as a second line of evidence that the 2L2S solution is correct. If, for example, we had somehow missed a 3L1S solution, and the derived 2L2S solution were merely mimicking it, then $q_{F,I} - q_{F,V}$ should be consistent with zero because there is only one source with just one color. However, according to Equation (4) this possibility is excluded at 4.4σ .

In the second step, we calibrate the color and magnitude. With the measured instrumental color and brightness of the source, $(V-I, I)$, and the RGC centroid, $(V-I, I)_{\text{RGC}} = (2.473, 16.918)$, together with the known de-reddened values of the RGC centroid, $(V-I, I)_{\text{RGC},0} = (1.060, 14.509)$ (Bensby et al. 2013; Nataf et al. 2013), the reddening and extinction corrected color and magnitude of the source are estimated by

$$(V-I, I)_0 = (V-I, I)_{\text{RGC},0} + \Delta(V-I, I), \quad (5)$$

where $\Delta(V-I, I)$ denote the offsets in the color and brightness of the source from the RGC centroid measured on the instrumental CMD. This results in

$$(V-I, I)_0 = \begin{cases} (0.876 \pm 0.043, 18.418 \pm 0.010) & \text{for } S_1, \\ (2.455 \pm 0.831, 21.734 \pm 0.053) & \text{for } S_2. \end{cases} \quad (6)$$

In Table 5, we summarize the values of $(V-I, I)_{\text{RGC}}$, $(V-I, I)_{\text{RGC},0}$, $(V-I, I)$, and $(V-I, I)_0$ for the primary and companion source stars.

According to the estimated color and magnitude, the fainter source, S_2 , is clearly an early-to-mid M dwarf. On the other hand, the brighter source, S_1 , presents something of a puzzle because its best-fit position lies in a relatively unpopulated portion of the CMD (see Figure 9). The most likely explanation is that its true position lies $(1.5 - 2.0)\sigma$ blueward of the best-fit position. That is, it is most likely a very late G dwarf or a very early K dwarf. Because the position of S_1 is consistent with lying in the normal bulge population at the $(1 - 2)\sigma$ level, we evaluate its angular radius using the measured values and normal error propagation.

In the third step, we estimate the angular source radius using the measured source color and brightness. For this, we first convert $V-I$ color into $V-K$ color using the color-color relation of Bessell & Brett (1988), and then estimate θ_* using the

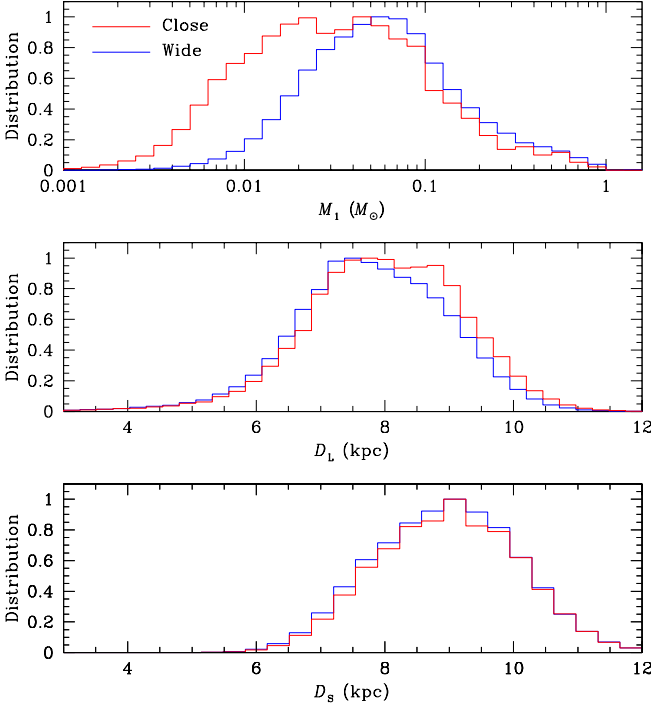


Fig. 10. Bayesian posteriors of the primary lens mass (M_1), and distances to the lens (D_L) and source (D_S). Red and blue curves are distributions obtained from the close and wide solutions, respectively.

($V - K$)– θ_* relation of Kervella et al. (2004). This process yields an angular source radius of

$$\theta_* = 0.803 \pm 0.066 \mu\text{as}. \quad (7)$$

We note that the source radius of S_2 is uncertain due to its large color uncertainty, and thus we use θ_* of S_1 for the θ_E estimation, i.e., $\theta_E = \theta_{*,1}/\rho_1$. With the angular source radius, the angular Einstein radius is estimated using the relation in Equation (2), which yields

$$\theta_E = \begin{cases} 0.056 \pm 0.005 \text{ mas} & (\text{close}), \\ 0.073 \pm 0.006 \text{ mas} & (\text{wide}). \end{cases} \quad (8)$$

Here the angular Einstein radius of the wide solution is scaled to θ_E^* . Together with the event timescale, the relative lens-source proper motion is estimated as

$$\mu = \frac{\theta_E}{t_E} = \begin{cases} 4.40 \pm 0.36 \text{ mas yr}^{-1} & (\text{close}), \\ 5.54 \pm 0.46 \text{ mas yr}^{-1} & (\text{wide}). \end{cases} \quad (9)$$

In Table 6, we summarize the values of θ_* , θ_E , and μ corresponding to the close and wide solutions.

5. Physical parameters of the lens and source

For KMT-2019-BLG-0797, it is difficult to uniquely determine the physical lens parameters because the microlens parallax cannot be measured due to the short timescale of the event, which is $\lesssim 5$ days. However, the lens parameters can still be constrained with the measured observables of the event timescale and angular Einstein radius, because these observables are related to the lens parameters by

$$t_E = \frac{\theta_E}{\mu}, \quad \theta_E = (\kappa M \pi_{\text{rel}})^{1/2}, \quad \pi_{\text{rel}} = \text{AU} \left(\frac{1}{D_L} - \frac{1}{D_S} \right). \quad (10)$$

Table 7. Physical lens parameters

| Parameter | Close | Wide |
|---------------------------|---------------------------|---------------------------|
| $M_1 (M_\odot)$ | $0.034^{+0.076}_{-0.024}$ | $0.064^{+0.107}_{-0.039}$ |
| $M_2 (M_\odot)$ | $0.021^{+0.043}_{-0.014}$ | $0.334^{+0.563}_{-0.204}$ |
| $D_L (\text{kpc})$ | $8.150^{+1.161}_{-1.161}$ | $7.725^{+1.188}_{-1.134}$ |
| $D_S (\text{kpc})$ | $9.147^{+1.092}_{-1.092}$ | $9.147^{+1.092}_{-1.092}$ |
| $a_{L,\perp} (\text{AU})$ | $0.258^{+1.438}_{-0.037}$ | $2.678^{+1.158}_{-0.401}$ |
| $a_{S,\perp} (\text{AU})$ | $0.097^{+0.014}_{-0.014}$ | $0.056^{+0.008}_{-0.008}$ |

Notes. M_1 denotes the lens component located closer to the source trajectory, not the heavier mass component.

Here $\kappa = 4G/(c^2 \text{AU})$, π_{rel} denotes the relative lens-source parallax, D_L and D_S represent the distances to the lens and source, respectively.

We estimate the physical lens parameters by conducting a Bayesian analysis. The analysis is done using the priors of the lens mass function and the physical and dynamical galactic models. We adopt the mass function models of Zhang et al. (2020) and Gould (2000), in which the former mass function includes stellar and brown-dwarf lenses and the latter one accounts for stellar remnants. The locations and motions of lenses and source stars are assigned using the physical distribution model of Han & Gould (2003) and the dynamical distribution model of Han & Gould (1995), respectively. Based on these models, we produce a large number (4×10^7) of artificial lensing events by conducting a Monte Carlo simulation, and then construct the distributions of the physical parameters. With the distributions, the representative values of the lens parameters are estimated as the median values of the distributions, and the uncertainties are estimated as the 16% and 84% ranges of the distributions.

Figure 10 shows the Bayesian posteriors of the primary lens mass and the distances to the lens and source. In Table 7, we list the estimated parameters M_1 , M_2 , D_L , D_S , $a_{L,\perp}$, and $a_{S,\perp}$. The last two parameters indicate the projected binary-lens and binary-source separations, that is,

$$a_{L,\perp} = s D_L \theta_E, \quad a_{S,\perp} = \Delta u D_S \theta_E, \quad (11)$$

where $\Delta u = \{[(t_{0,1} - t_{0,2})/t_E]^2 + (u_{0,1} - u_{0,2})^2\}^{1/2}$ is the instantaneous separation between S_1 and S_2 at the time of the lensing magnification.

According to the close solution, the lens is composed of two brown dwarfs with masses $(M_1, M_2) \sim (0.034, 0.021) M_\odot$ located in the bulge with a distance of $D_L = 8.2^{+1.2}_{-1.2}$ kpc. According to the wide solution, on the other hand, the lens is composed of an object at the star/brown-dwarf boundary and an M dwarf with masses $(M_1, M_2) \sim (0.06, 0.33) M_\odot$, and it is located at a distance of $D_L = 7.7^{+1.2}_{-1.1}$ kpc. The masses of M_1 estimated from the close and wide solutions are similar to each other, although the wide solution prefers somewhat larger mass due to the larger value of the estimated θ_E . On the other hand, the masses of M_2 estimated from the two degenerate solutions are widely different from each other. This is because M_1 and M_2 have similar masses, with $q \sim 0.6$, according to the close solution, while M_2 according to the wide solution is much heavier than M_1 , with $q \sim 5.3$. For both the close and wide solutions, the source is located slightly behind the galactic center at a distance of $D_S \sim 9.1$ kpc. This is because source stars located in the far side of the bulge have higher chances to be lensed than stars located in the front side. The projected separations between the lens and source components are $(a_{L,\perp}, a_{S,\perp}) \sim (0.26, 0.10)$ AU according to the close solution, and $\sim (2.68, 0.06)$ AU according to the wide solution. We note that the expected orbital pe-

riod of the source, $P \gtrsim 10.5$ days for the close solution and $P \gtrsim 5$ days for the wide solution with the source mass of $M_S = M_{S_1} + M_{S_2} \sim 0.9 M_\odot + 0.3 M_\odot \sim 1.2 M_\odot$, is short, and thus the orbital motion of the source may affect the lensing light curve. However, it is difficult to constrain the orbital motion first because the duration of the anomaly, which is ~ 1 day, is much shorter than the orbital period, and second because the photometric precision in the wings of the light curve is not good enough to capture the small modulations induced by the source orbital motion.

6. Summary and conclusion

We investigated the lensing event KMT-2019-BLG-0797, for which the light curve was found to be anomalous from the reexamination of events detected in and before the 2019 season. For this event, it was found that a 2L1S model could not explain the anomaly. From the tests with various models, it was found that the anomaly could be explained by introducing an extra source star to a 2L1S model. The event is the third case of a confirmed 2L2S event following on MOA-2010-BLG-117 (Bennett et al. 2018) and OGLE-2016-BLG-1003 (Jung et al. 2017).

The interpretation of the light curve was subject to a close-wide degeneracy. According to the close solution, the lens is a binary consisting of two brown dwarfs with masses $(M_1, M_2) \sim (0.034, 0.021) M_\odot$, and it is located at a distance of $D_L \sim 8.2$ kpc. According to the wide solution, on the other hand, the lens is composed of an object at the star/brown-dwarf boundary and an M dwarf with masses $(M_1, M_2) \sim (0.06, 0.33) M_\odot$ located at $D_L \sim 7.7$ kpc. The binary source is comprised of a primary near the G-dwarf/K-dwarf boundary and an early-to-mid M dwarf companion.

Acknowledgements. Work by C.H. was supported by the grants of National Research Foundation of Korea (2019R1A2C2085965 and 2020R1A4A2002885). This research has made use of the KMTNet system operated by the Korea Astronomy and Space Science Institute (KASI) and the data were obtained at three host sites of CTIO in Chile, SAAO in South Africa, and SSO in Australia.

References

Alard, C., & Lupton, R. H. 1998, *ApJ*, 503, 325
 Albrow, M. 2017, MichaelDAIbrow/pyDIA: Initial Release on Github, Version 1.0.0, Zenodo, doi:10.5281/zenodo.268049
 Albrow, M., Horne, K., Bramich, D. M., et al. 2009, *MNRAS*, 397, 2099
 Becker, A., Alcock, C., Allsman, R., et al. 1997, *Bulletin of the American Astronomical Society*, 29, 1347
 Bennett, D. P. 2010, *ApJ*, 716, 1408
 Bennett, D. P., Rhie, S. H., Nikolaev, S., et al. 2010, *ApJ*, 713, 837
 Bennett, D. P., Rhie, S. H., Udalski, A., et al. 2016, *AJ*, 152, 125
 Bennett, D. P., Udalski, A., Han, C., et al. 2018, *AJ*, 155, 141
 Bensby, T., Yee, J. C., Feltzing, S., et al. 2013, *A&A*, 549, A147
 Bessell, M. S., & Brett, J. M. 1988, *PASP*, 100, 1134
 Bozza, V., Bachelet, E., Bartolici, F., Heintz, T. M., Hoag, A. R., & Hundertmark, M. 2018, *MNRAS*, 479, 5157
 Bozza, V., Dominik, M., Rattenbury, N. J., et al. 2012, *MNRAS*, 424, 902
 Bond, I. A., Abe, F., Dodd, R. J., et al. 2001, *MNRAS*, 327, 868
 Bond, I. A., Rattenbury, N. J., Skuljan, J., et al. 2002, *MNRAS*, 333, 71
 Chang, K., & Refsdal, S. 1979, *Nature*, 282, 561
 Chang, K., & Refsdal, S. 1984, *A&A*, 132, 168
 Dominik, M., & Hirshfeld, A. C. 1994, *A&A*, 289, L31
 Dong, S., Bond, I. A., Gould, A., et al. 2009, *ApJ*, 698, 1826
 Gaudi, B. S., Bennett, D. P., Udalski, A., et al. 2008, *Science*, 319, 927
 Gould, A. 2000, *ApJ*, 535, 928
 Gould, A., & Gaucherel, C. 1997, *ApJ*, 477, 580
 Gould, A., & Loeb, A. 1992, *ApJ*, 396, 104
 Gould, A., Udalski, A., Shin, I.-G., et al. 2014, *Science*, 345, 46
 Griest, K., & Hu, W. 1992, *ApJ*, 397, 362
 Han, C., Bennett, D. P., Udalski, A., et al. 2019, *AJ*, 158, 114
 Han, C., & Gould, A. 1995, *ApJ*, 447, 53

Han, C., & Gould, A. 2003, *ApJ*, 592, 172
 Han, C., Kim, D., Jung, Y. K., et al. 2020a, *AJ*, 160, 17
 Han, C., Lee, C.-U., Udalski, A., et al. 2020b, *AJ*, 159, 48
 Han, C., Shin, I.-G., Jung, Y. K., et al. 2020c, *A&A*, 641, A105
 Han, C., Udalski, A., Choi, J.-Y., et al. 2013, *ApJ*, 762, L28
 Han, C., Udalski, A., Gould, A., et al. 2017, *AJ*, 154, 223
 Han, C., Udalski, A., Kim, D., et al. 2020d, *A&A*, 642, A110
 Han, C., Udalski, A., Kim, D., et al. 2020e, *A&A*, submitted
 Han, C., Udalski, A., Lee, C. U., et al. 2020f, *AJ*, 159, 48
 Han, C., Udalski, A., Lee, C. U., et al. 2020g, in preparation
 Han, C., Udalski, A., Lee, C. U., et al. 2020h, *A&A*, submitted
 Holtzman, J. A., Watson, A. M., Baum, W. A., et al. 1998, *AJ*, 115, 1946
 Hwang, K.-H., Choi, J.-Y., Bond, I. A., et al. 2013, *ApJ*, 778, 55
 Hwang, K.-H., Han, C., Bond, I. A., et al. 2010, *ApJ*, 717, 435
 Hwang, K.-H., Udalski, A., Bond, I. A., et al. 2018, *AJ*, 155, 259
 Jung, Y. K., Udalski, A., Bond, I. A., et al. 2017, *ApJ*, 841, 75
 Kervella, P., Thévenin, F., Di Folco, E., & Ségransan, D. 2004, *A&A*, 426, 29
 Kim, S.-L., Lee, C.-U., Park, B.-G., et al. 2016, *JKAS*, 49, 37
 Kim, H.-W., Hwang, K.-H., Shvartzvald, Y., et al. 2018, *AAS*, submitted [arXiv: 1806.07545]
 Mao, S., & Paczyński, B. 1991, *ApJ*, 374, L37
 Nataf, D. M., Gould, A., Fouqué, P., et al. 2013, *ApJ*, 769, 88
 Nishiyama, S., Nagata, T., Tamura, M., Kandori, R., Hatano, H., Sato, S., & Sugitani, K. 2008, *ApJ*, 680, 1174
 Poleski, R., Skowron, J., Udalski, A., et al. 2014, *ApJ*, 795, 42
 Ryu, Y.-H., Han, C., Hwang, K.-H., et al. 2010, *ApJ*, 723, 81
 Ryu, Y.-H., Udalski, A., Yee, J. C., et al. 2020, *AJ*, 160, 183
 Suzuki, D., Bennett, D. P., Udalski, A., et al. 2018, *AJ*, 155, 263
 Tomaney, A. B., & Crotts, A. P. S. 1996, *AJ*, 112, 2872
 Udalski, A., Szymański, M., Mao, S., Di Stefano, R., Kaluźny, J., Kubiak, M., Mateo, M., & Krzemiński, W. 1994, *ApJ*, 436, L103
 Udalski, A., Szymański, M. K., & Szymański, G. 2015, *Acta Astron.*, 65, 1
 Yee, J. C., Shvartzvald, Y., Gal-Yam, A., et al. 2012, *ApJ*, 755, 102
 Yoo, J., DePoy, D. L., Gal-Yam, A., et al. 2004, *ApJ*, 603, 139
 Zhang, X., Zang, W., Udalski, A., et al. 2020, *AJ*, 159, 116